

# Vortex Wake Geometry of a Model Tilt Rotor in Forward Flight

Gloria K. Yamauchi  
gyamauchi@mail.arc.nasa.gov  
Aerospace Engineer  
NASA Ames Research Center  
Moffett Field, California, USA

Wayne Johnson  
wrjohnson@mail.arc.nasa.gov  
Aerospace Engineer  
NASA Ames Research Center  
Moffett Field, California, USA

Alan J. Wadcock  
awadcock@mail.arc.nasa.gov  
Principal Scientist  
Aerospace Computing Inc.  
Moffett Field, California, USA

## Abstract

The vortex wake trajectory from one rotor of a 0.25-scale V-22 tiltrotor model was measured for four test conditions in the NASA Ames 40- by 80-Foot Wind Tunnel. Vortex wake images were acquired using a laser light sheet and video camera. Wake trajectories were constructed by extracting vortex positions from the video images. Wake trajectories were also calculated using the comprehensive analysis CAMRAD II. Measured and calculated wake geometries exhibit similar trends when advance ratio is varied at fixed thrust or when thrust is varied at fixed advance ratio.

## Notation

A	rotor disk area, $\pi R^2$
$C_T$	rotor thrust coefficient, thrust/ $(\rho(\Omega R)^2 A)$
$M_{tip}$	blade tip Mach number, $\Omega R / \text{sound speed}$
R	blade radius
$\mu$	advance ratio, tunnel speed/ $\Omega R$
$\Omega$	rotor rotational speed
$\rho$	air density
$\Psi_b$	azimuth position of reference blade relative to laser sheet

## Introduction

The aerodynamics of a tiltrotor blade can be vastly different than a conventional helicopter blade. Compared to a helicopter blade, tiltrotor blades have a higher built-in twist, higher solidity, and higher disk loading. These differences result in very different blade load distributions. For this reason existing analytical and empirical models developed for helicopter rotors do not necessarily apply to tiltrotors. In particular, wake geometry models for helicopters are inadequate for tiltrotor wake systems. In both level flight and descent conditions where blade-vortex interaction (BVI) occurs, tiltrotor blades can undergo negative tip loading over a substantial region of the rotor disk unlike conventional helicopter blades. The negative tip-loading causes dual vortices, of opposite sign, to be shed from a single blade. The dual vortices greatly complicate the wake geometry and present a challenge to the analyst trying to model the wake.

In 1998, an isolated 0.25-scale tiltrotor was tested in the Duits-Nederlandse Windtunnel Large Low-Speed Facility (Ref. 1). The model was the Tilt Rotor Aeroacoustic Model (TRAM). During this aeroacoustic test, wake geometry measurements and wake velocity field measurements were acquired on the advancing side of the rotor disk (Ref. 2). The flow measurements revealed, for the first time, the complicated geometry of the tiltrotor wake. Counter-rotating vortex pairs were clearly evident, but the age and origin of the vortices were not determined in the limited test time available.

Recent correlation efforts using CAMRAD II and airloads data from the TRAM rotor highlighted the inadequacies of conventional helicopter wake models for predicting tiltrotor aerodynamics (Refs. 3-4). A new wake model designed to capture the complexities of a tiltrotor wake was therefore developed (Ref. 5) for CAMRAD II.

In late 2000, the isolated TRAM rotor was incorporated into a full-span tiltrotor model and tested in the NASA Ames 40- by 80-Foot Wind Tunnel. Extensive planning and preparation for wake geometry and velocity field measurements (using Particle Image Velocimetry (PIV)) preceded the test. Since wake age was not measured during the isolated rotor test, the objectives of the full-span wake geometry measurements were to identify the location along the blade span where the dual vortices formed and to record the location of the vortex pair as a function of rotor azimuth. Flow visualization using a laser light sheet (LLS) would be used to achieve this goal. PIV would then be used to measure size and strength of selected vortices. Test conditions were selected to match the isolated rotor flow measurement conditions of Ref. 2. Unfortunately, the test in the 40- by 80-Foot Wind Tunnel ended prematurely due to failure of a lubrication system and no PIV data were obtained. Limited wake geometry measurements were acquired, however, and these data are the subject of this paper.

*Presented at Heli Japan 2002, AHS International Meeting on Advanced Rotorcraft Technology and Life Saving Activities, Tochigi, Japan, November 11-13, 2002.*  
Copyright © 2002 by the American Helicopter Society International, Inc. All rights reserved.

This paper provides a detailed description of the experimental set-up used to acquire the wake images and the subsequent analysis of the images. Details of the CAMRAD II tiltrotor wake models are described. Comparisons between the measured and calculated vortex locations are presented and discussed for four test conditions.

### Facility and Model Description

The 40- by 80-Foot Wind Tunnel at NASA Ames Research Center is a closed-circuit, single-return tunnel driven by six 40-foot diameter fans. The test section is acoustically treated and measures 39-feet high, 79-feet wide, and 80-feet long. The maximum speed of the tunnel is approximately 270 knots.

NASA's Tilt Rotor Aeroacoustic Model (TRAM) is a nominal quarter-scale representation of the V-22 aircraft. The TRAM can be configured as an isolated rotor or a full-span aircraft. Each 3-bladed rotor has a diameter of 9.5 feet. The full-span configuration has dual powered rotors with manually adjusted nacelle tilt. Model measurements include blade structural loads, blade airloads, individual rotor forces and moments, fuselage forces and moments, and wing static pressures. Further details about the TRAM are reported in Refs. 6-8. Figure 1 shows the TRAM installed in the Ames 40- by 80-Foot Wind Tunnel.

### Experimental Set-Up for Flow Measurements

The large size of the test section combined with limited optical access presents a challenge for the successful implementation of optical techniques. The planned PIV acquisition requirements dictated the camera and laser set-up which were also used for wake geometry measurements. If wake geometry measurements alone were planned, a less complex set-up would have been implemented.

In order to identify the spanwise location of the dual-vortex formation, a vertical light sheet corresponding to a blade azimuth angle close to 90 degrees on the advancing side of the left-hand rotor disk was chosen for the current study. The placement of the light sheet at the left-hand rotor was necessary given the limited choices for locating the laser, optics, and cameras. The laser beam was introduced into the test section from the right-hand-side of the test section (pilot's viewpoint). Figure 2 illustrates the launch of the laser sheet into the test section from a specially constructed wall cavity at the required streamwise station. The laser sheet passed above the RH rotor (pilot's view) and immediately downstream of the spinner on the LH rotor in order to reach the outboard half of the rotor disk where the measurements were made on the advancing blade. The white rectangle in Fig. 2 indicates the camera field of view.

### Laser and Laser Sheet Optics

The laser was placed on an optical table located on a wide external platform outside the test section on the right-hand-side of the tunnel (pilot's view). The laser is a Spectra Physics PIV400 dual-oscillator Nd:Yag laser with 350 mJ/pulse at 532nm wavelength. Laser pulse duration is 9 ns. For the TRAM tip radius of 4.75 ft the desired tip Mach number of 0.63 corresponds to a 1/rev frequency of about 23.58 Hz. The maximum repetition rate for the laser is 15 Hz, therefore the rotor 1/rev pulse train was divided by 2 giving an acceptable laser trigger rate of 11.79 Hz. The laser was tuned to operate at a frequency of 11.8 Hz  $\pm$  1 Hz, thereby providing sufficient margin for day-to-day variations in the speed of sound caused by ambient temperature changes.

A test section wall cavity was modified to house the necessary LLS optics. Beam-steering mirrors and optics for spreading the laser sheet were rail-mounted inside the wall cavity to simplify streamwise adjustment of the laser sheet position.

### Laser Sheet Alignment

The vertical laser sheet was positioned cross-stream at a suitable streamwise location so as to graze the blade trailing edge with the blade at a nominal angle of 90 degrees. The procedure for locating the sheet is described next.

The TRAM model was pre-positioned with the nacelles at 85 degrees and the fuselage angle-of-attack at +11 degrees (nose up). The resulting tip-path-plane was at 6 degrees nose up. The rotor gimbal lock was installed on the LH rotor and the LH rotor manually rotated until the primary blade was close to 90 degrees blade azimuth. A vertical plane was established in the test section using an industrial He-Ne laser level. This vertical plane was then adjusted to be perpendicular to the tunnel axis using acoustic panels on opposite walls of the test section as markers. Reference drawings for the wind tunnel indicate a maximum allowable error in wall panel placement of  $\pm 1/4$  inch. This implies a maximum error in placement of the cross-stream laser sheet of  $\pm 1/2$  inch in 79 ft, or  $\pm 0.030$  degrees. Using the reference marks on the tunnel wall, the laser level was then adjusted in the streamwise direction until the sheet grazed the blade trailing edge over the outboard half of the blade. Markers were placed on the tunnel wall to identify this reference plane. The laser level was then turned off and the Nd:Yag laser launched into the test section. The focused sheet (about 1 mm-thick) was positioned about 2 mm downstream of the blade trailing edge (over the outermost 50% of the blade radius). The focus was then translated outboard of the blade tip in order to produce a 4-mm thick sheet in the area of interest, satisfying the requirements for the planned PIV measurements. The resulting LLS was 4-mm thick, grazing the blade trailing edge, with the LLS in the vertical plane precisely perpendicular

to the tunnel axis. The markers on the tunnel wall identifying the reference plane were continually used to check for any obvious drift in the laser sheet.

#### Camera

Figure 3 shows the installation of the LLS camera in the camera port on the left side of the tunnel. The TRAM is seen in the background through the window. Cantilevered to the side of the pan-and-tilt stage is a strobe and above is the LLS camera. The camera is a Hitachi KP-FIU with Fujinon 75 mm lens at F4.0 with automatic gain control. The camera was carefully positioned using the remote-control pan-and-tilt stage and focus was set manually. The two boxes on the left inside the wall cavity are the strobe power supply sitting on top of the pan-and-tilt controller. All this equipment was designed to roll out on a pair of rails to simplify access. The window is made from 1/4-inch float glass.

#### LLS Camera Calibration

The camera calibration target consisted of a 9 x 9 rectangular grid with mesh size 4 inches vertical by 8 inches radial. The 3 ft x 6 ft target was large enough to span from inside the blade root to outside the blade tip. The target was suspended vertically from an aistand and aligned with the laser sheet so that the laser sheet washed over the front face of the calibration image. Once in position, the laser was turned off and a short video sequence acquired from the LLS camera. A group of 250 video frames was then averaged to produce a single image that was used to convert image space to physical space. Grid locations determined from the averaged image were tabulated and curve fit to the known physical grid coordinates in the following manner:

$$Y = f(x_p, y_p)$$

$$Z = g(x_p, y_p)$$

where Y and Z represent physical space coordinates (inches) and  $x_p$  and  $y_p$  represent image space (pixels). A bi-quadratic curve fit was performed resulting in a standard deviation for the residual errors in the Y-direction of 0.06 inch. The equivalent value for the Z-direction was 0.02 inch. Typical scale in the camera image was 17 pixels/inch in the vertical direction and 8.5 pixels/inch in the horizontal direction. Maximum uncertainty in identifying the grid location in the calibration image was  $\pm 1$  pixel. This corresponds to  $\Delta Y = 0.12$  inch and  $\Delta Z = 0.06$  inch. The errors in the camera calibration were therefore consistent with the estimated uncertainty in the grid point locations.

The gimbaled hub presented a problem when trying to use the stationary rotor tip as the coordinate origin. To simplify matters, the "on condition" blade tip location was used as the reference origin.

#### Flow Seeding

Successful LLS flow visualization requires highly non-uniform seed distribution in the area of interest. For this test, the rotor tip path plane was approximately 2.5 ft above the tunnel centerline. In order to deliver the seed at the desired height, the most economical (in terms of cost and effort) solution was to position a 70-foot work stand downstream of the fan drive. The work stand was a significant distance upstream from the test section. Two Corona mineral oil seeders were mounted on the work stand. By varying the height of the work stand, adequate adjustment of the smoke release point was obtained. During the flow visualization run, the tunnel air exchange door was open 100% (10% air exchange) in order to limit the background level of the smoke, thereby maintaining maximum contrast in the LLS images between seeded and unseeded flow.

#### Data Acquisition

The primary data acquisition system for the flow visualization data was a Sony DHR-1000 digital video cassette recorder with internal time code generator (HH:MM:SS:FF). As backup, the analog video signal was also routed to a JVC S-VHS VCR model HR-S4600U. The video was simultaneously displayed on a video monitor for real-time display and control of the smoke injection.

The flow visualization study was planned to occur in two stages. During the first stage, each of the 4 test conditions was documented on video in "slip synch" mode. The laser was triggered at a fixed frequency slightly different from the rotor rpm (actually rotor rpm/2) which caused the rotor blade to slowly precess through the video frame. During motor testing prior to tunnel entry the feedback loop on the motor had been optimized to provide a perfectly steady rotor rpm. Unfortunately, during the wind tunnel test (presumably with a different operating point for the motor) this was not the case despite adjustments to the feedback loop. As a result of rotor rpm variations, it was not possible to assign vortex age to any single video frame apart from those frames where the blade trailing edge lies in the laser sheet. This does not prevent the documentation of the vortex trajectory, however, and this was the main goal. Four test conditions were documented in slip-synch mode (two thrust levels each at  $\mu = 0.10$  and  $\mu = 0.15$ ) over a period of about 20 minutes. The second stage of the flow visualization study called for additional documentation of the wake geometry from acquisition of video segments at constant blade azimuth with respect to the laser sheet, in increments of 15 degrees of blade motion. Unfortunately, model failure curtailed the run at the conclusion of the slip-synch portion of the study and no second stage measurements were acquired.

### Post-Test Data Processing

The analog video signal was a standard 30-frames/sec (60 interlaced fields) black and white video stream. With the laser pulse rate of 11.79 Hz, only about 12 of the 30 video frames in each second contained useful information. The other 18 images were blank. Four to six minutes of video stream were recorded for each of the four test conditions. All LLS flow visualization images were transferred to computer hard disk for subsequent analysis. All blank frames were removed for efficiency in data storage. Video playback and analysis were performed using NIH Image, a public domain image-processing program developed by the National Institutes of Health (<http://rsb.info.nih.gov/nih-image/>).

The primary goal of the data processing was to determine the coordinates of the vortices in the plane of the laser sheet. This was accomplished using the following procedure for each test condition. First, the video frames were repeatedly viewed in succession as a movie to identify the vortical structures and determine the general trajectory of the vortices. Next, the vortex location in pixel space and the vortex rotation direction were tabulated frame by frame. For a given frame, there may be as many as 3-4 identifiable vortices or there may be none. After processing about 2 minutes of video, representing approximately 1440 frames, the data were plotted to determine whether there were enough data points to define a vortex trajectory. Additional frames were processed until a well-defined trajectory was obtained. The next step was to assign an azimuth position  $\Psi_b$  (nondimensional time) to each vortex. This required another pass through the data. The reference time  $\Psi_b$  is the azimuth angle of the reference blade corresponding to the identified intersection of the wake with the laser light sheet. For the calculated wake geometry, this time (and indeed the actual wake age) is available for all intersections. For the measured wake geometry,  $\Psi_b$  can only be assigned for those frames where the blade trailing edge was coincident with the laser sheet, hence only when  $\Psi_b$  is a multiple of 120 degrees. Note that blade azimuth is defined by the location of the pitch axis and not the blade trailing edge, and so for  $\Psi_b = 0$  the blade azimuth is close to 90 degrees but not necessarily equal to 90 degrees.

### Uncertainty in Extracting Vortex Location

The best indication of the vortex center was provided by a particle void. The presence of a particle void provided an objective measurement of the vortex center with maximum error of  $\pm 0.5$  pixel ( $\Delta Y = 0.06$  inch and  $\Delta Z = 0.03$  inch). If no particle void was evident, the measurement of vortex location became highly subjective and measurement uncertainty increased correspondingly. Without a particle void we were forced to identify the apparent center of any "circular" smoke mass as the vortex center. In general the smoke feature had an elliptic cross-section due to

oblique camera observation angle and/or vortex filament angle with respect to the plane of the LLS. On occasion, internal features were used to identify the vortex center (either reduced or increased smoke density) leading us to identify some point other than the smoke centroid as the vortex center. There were no definitive rules and the measurement could be highly subjective.

In general, the size of the swirling smoke mass used to define the vortex grows as the vortex ages. If the center of this rotating smoke mass was identified as the vortex center then the uncertainty in the measurement of vortex location increased linearly with the size of the smoke mass. Each individual measurement had a high degree of uncertainty. However, by analyzing many video frames, the number of vortex location measurements was increased sufficiently to define the mean vortex trajectory with high confidence. A reasonable estimate for the maximum uncertainty in determining the vortex center was  $1/2$  the radius of the smoke mass. Based on the size of the typical vortex swirl pattern used to determine the vortex center, the maximum uncertainty in either radial or vertical location was about  $\pm 1$  inch. This was also the typical scatter found in the observations. The scatter in the vortex trajectory data, therefore, may be due to vortex wander or due to the uncertainty in locating the vortex center when no particle void was present. Assuming a normal distribution of the vortex location within the smoke mass gives a standard deviation of about  $1/3$  inch in either direction. The assumption that the vortex center can be identified by the "centroid" of some mass of swirling smoke could be erroneous, however. There may be a deterministic error present in such a determination of vortex location. All we know with certainty was that the vortex center was located somewhere within the smoke mass. Figure 4 shows a representative video frame. The location of the blade trailing edge when passing through the sheet is identified along with the location of the tip trailing edge. In this particular frame, three vortices are identified. Other vortical structures may be present in the image, but unless the structure is consistently present and clearly swirling, the structure was excluded as a vortex.

### **Analysis**

The rotorcraft comprehensive analysis CAMRAD II was used to calculate wake geometries for the four conditions for which measured wake geometry is available. CAMRAD II is an aeromechanical analysis of helicopters and rotorcraft that incorporates a combination of advanced technologies, including multibody dynamics, nonlinear finite elements, and rotorcraft aerodynamics. The trim task finds the equilibrium solution (constant or periodic) for a steady state operating condition, in this case a single rotor

operating in a wind tunnel. Calculations for a single rotor, rather than a dual rotor system, were appropriate for this study since the region of interest was the near wake which is assumed to be unaffected by the presence of the other rotor. Also, computational time was greatly reduced by modeling three blades rather than six. For wind tunnel operation, the thrust and flapping (longitudinal and lateral gimbal tilt) were trimmed to measured values. The aerodynamic model includes a free wake analysis to calculate the rotor nonuniform induced-velocities. CAMRAD II is described in Refs. 9 to 13.

#### Tiltrotor Wake Model

The CAMRAD II rotor wake analysis uses second-order lifting line theory, with the general free wake geometry calculation described in Refs. 12 and 13. Two tiltrotor wake models are described in Refs. 3 and 4, characterized as the rolled-up and the multiple-trailer models.

The rolled-up model uses a dual-peak representation to accommodate negative tip loading. The tip vortex, with a core radius of 20% mean chord, is defined by the negative tip-loading. The positive trailed vorticity inboard of the negative tip loading rolls up with a core radius of 30% mean chord. There is partial entrainment of the trailed vorticity into the tip vortex. The dual-peak model is only used at azimuths where the negative loading extends inboard to at least 0.945R.

The multiple-trailer model has a discrete trailed vortex line emanating from each blade aerodynamic panel edge. Although the multiple-trailer model provides good correlation of calculated and measured airloads of an isolated tiltrotor, the performance correlation was unsatisfactory. The multiple-trailer model was therefore modified to incorporate a simulation of the tip vortex formation process (Ref. 5). In the modified model, known as the multiple-trailer with consolidation, the trailed vortex lines at the panel edges are combined into rolled-up vortices using the trailed vorticity moment to scale the rate of roll-up. All the vorticity in adjacent vortex lines having the same sign eventually rolls up into a single vortex located at the centroid of the vorticity distribution. Reference 5 showed that adding the consolidation feature improved the performance correlation while maintaining good airloads correlation. The consolidation feature was therefore used with the multiple-trailer model in this study.

#### **Results**

Measured and calculated wake geometries are presented for the four test conditions provided in Table 1. All data were acquired for a rotor tip path plane angle of 6 deg (shaft tilted aft) and approximately zero 1/rev flapping. The experimental results are presented first, followed by the CAMRAD

II calculations. Comparisons between the measured and calculated wake geometries are then discussed.

Table 1. Test Conditions

Case	$C_T$	$\mu$	$M_{tip}$
A	0.0087	0.150	0.630
B	0.0125	0.150	0.630
C	0.0087	0.099	0.629
D	0.0127	0.099	0.630

#### Experimental Results

The following points must be kept in mind as the data are discussed:

1. The left-hand rotor under investigation rotates in a CW (clockwise) sense when viewed from above.
2. The laser light sheet is at a nominal blade azimuth of 90 degrees, on the advancing side of the rotor disk.
3. The rotor blade height is rising for the first 90 degrees of blade motion after passing through the laser sheet.
4. Each vortex wake is viewed from behind, looking upstream.
5. The coordinate system for the data plots is based on the location of the trailing edge of the blade at the blade tip as the blade trailing edge passes through the laser sheet.
6. Positive lift on the blade produces a vortex with clockwise (CW) rotation. Negative blade lift produces a vortex with counter-clockwise (CCW) rotation.

The measured and calculated data are presented in terms of intersections of the trailed vortices with the laser light sheet. Each figure shows the intersections for many time steps. The intersections are identified by the azimuth position  $\Psi_b$  (nondimensional time) of the reference blade relative to the laser light sheet. So  $\Psi_b=0$  corresponds to the blade just ahead of the sheet, while  $\Psi_b=120$  deg has the blade 1/3 revolution later and the following blade just ahead of the sheet. A trailed wake bundle that rolls up at radial station  $r$  and intersects the sheet with age  $\phi$ , has been convected longitudinally by a distance approximately  $r\sin\phi=\mu\Psi_b$ ; hence the age of an intersection is  $\phi = \sin^{-1}(\mu\Psi_b/r)$ . For example, when  $\Psi_b=120$  deg a trailed vortex filament from the tip ( $r=1$ ) that intersects the sheet is only  $\phi=12$  or 18 deg old (that is, created then the blade is 12 or 18 deg forward of the sheet) for  $\mu=0.10$  or 0.15, respectively. A trailed vortex filament created at the tip ( $r=1$ ) when the blade is 45 deg ahead of the sheet will intersect the sheet after about 1.10 or 0.75 revolutions ( $\Psi_b=405$  or 270 deg) for  $\mu=0.10$  or 0.15, respectively. The rotation of the blades creates trailed vortex lines that are skewed in the horizontal plane, hence as they are convected aft their intersections with the laser light

sheet move laterally. The vertical distortion of the trailed lines produces vertical motion of the intersections. Thus the lateral and vertical motion (as  $\Psi_b$  increases) of the intersections at the laser light sheet reflect the skewed geometry of the lines being convected downstream past the sheet.

For a tip path plane angle of 6 deg, ignoring cyclic pitch, the blade tip was 5.96 inches higher at the front of the rotor disk (blade azimuth = 180 deg) than at an azimuth of 90 degrees (laser sheet location). One degree of cyclic pitch corresponds to a vertical motion of the blade trailing edge of about 0.072 inches. Neglecting dynamic effects, blade motion due to cyclic pitch should have a very small effect on the vortex location.

Figures 5-8 present the measured vortex locations and Figs. 9-12 are representative images for each of the four test conditions. The origin for the plots in Figures 5-8 is indicated on the images of Figs. 9-12. A discussion of each test condition follows.

**Case A:  $C_T = 0.0087, \mu = 0.150$ .** Measurements of vortex trajectory for test condition A are shown in Fig. 5. The lack of data close to the origin indicates a possible slow roll-up of what is clearly seen to be a CCW vortex associated with negative blade loading at the blade tip. A corresponding wake image is provided in Fig. 9. The trajectory of this vortex can be followed with high confidence (confirmed by the low degree of scatter) for a complete rotor revolution. Also visible in Fig. 5 is a cluster of points showing the trajectory of a CW vortex assumed to develop from an inboard station. The roll up of the CW vortex occurs for  $\Psi_b > 120$  degrees. Vortices that arise from radial stations other than the blade tip are difficult to identify with a particular blade. The upright "mushroom" flow pattern identifiable in the flow visualization image of Fig. 9 is consistent with an outboard CCW vortex (negative blade loading at the blade tip) and an inboard CW vortex (positive blade loading inboard). These flow patterns were also reported in Ref. 2.

**Case B:  $C_T = 0.0125, \mu = 0.150$ .** Based on airloads measurements reported in Ref. 2, we know that negative tip loading for this condition is not as prevalent over the azimuth compared with the lower thrust condition of Case A. The blade tip at 90 deg azimuth for Case B is positively loaded (compared to the negative tip loading of Case A) as shown by the CW vortex shed from the tip in Fig. 6. For  $\Psi_b < 120$  deg, the CW tip vortex first appears at the blade tip only to disappear from view and reappear slightly inboard, suggesting the positive blade loading has moved inboard from the tip. At about  $\Psi_b = 240$  deg, an upright mushroom pattern associated with a CCW vortex originating at the blade tip and a CW vortex originating inboard becomes visible. The wake images for this condition (Fig. 10) show a mushroom pattern that convects in an upright position. As a

result, there is little difference in height between the CW and CCW vortex trajectories of Fig. 6. Case A, in comparison, shows the CCW vortex trajectory was at least 2.5 times higher than the CW vortex trajectory. Although hundreds of images were reviewed for this case, there is a CW vortex which could not be assigned a value of  $\Psi_b$ . This CW vortex is located about mid-span and slightly above the blade (Fig. 6). One explanation for this CW vortex is that the blade spanwise loading produces a counter-rotating vortex pair near the tip plus a CW vortex further inboard. The wake of Case B is more chaotic than that of Case A, which results in a higher degree of scatter in Fig. 6 than Fig. 5.

**Case C:  $C_T = 0.0087, \mu = 0.099$ .** Figure 7 shows the measured vortex trajectories for Case C and Fig. 11 shows a typical wake pattern. The trajectory of the CCW vortex shed from the blade tip is very similar to Case A. More noticeable, however, is the complete lack of evidence of any rolled-up vortex immediately following blade passage through the laser sheet. Based on a comparison with Case A, the first appearance of a vortex is probably well after first blade passage. This lack of information implies that the trailed vorticity at the blade tip is slow to roll up, or is weak, or both. Scatter in the data is quite low indicating a high degree of repeatability. Clockwise vortices that are shed inboard from the blade tip appear to congregate in separate groups beneath the path of the CCW tip vortex. The mushroom flow pattern (Fig. 11) is initially upright for  $120 \text{ deg} < \Psi_b < 240 \text{ deg}$  at which point the pattern rotates into a vertical (CCW vortex above CW vortex) orientation as the vortices age further.

**Case D:  $C_T = 0.0127, \mu = 0.099$ .** For Case D, there is little negative loading at the blade tip over the azimuth, as shown by the near absence of negative (CCW) vortices. Figure 8 shows the wake trajectory for this case and Fig. 12 shows a representative wake pattern. This wake pattern is typical of a helicopter blade loading, that is, the overwhelming presence of positive CW vortices.

As the rotor blade passes through the LLS a strong CW vortex is seen to originate slightly inboard of the blade tip. The vortex center is easily determined from a visible particle void (Fig. 12). As the blade moves upstream of the laser sheet, the trailed vortex moves rapidly higher as it moves slowly inboard. Sometime before the following blade reaches the laser sheet, a weak secondary vortex can be discerned outboard and above the primary tip vortex. This CCW vortex is assumed to be a bi-product of a negative tip loading that has occurred as the blade moved upstream of the 90 deg azimuth position. This vortex is claimed to be weak because the only evidence of its existence is the particle-void in the laser sheet and because no direct evidence for the sense of rotation of this vortex is provided by any

adjacent smoke. The local flow is totally dominated by the primary CW vortex. The existence of the secondary vortex is apparently short-lived. By the time the following blade reaches the laser sheet the secondary vortex has disappeared. At large vortex age, the primary vortex descends as it moves inboard towards the blade root.

Figure 8 shows little scatter in the data, indicating the high level of confidence in the measurement and the high degree of repeatability in the vortex trajectory from rev-to-rev. Note the high confidence in the vortex trajectory up to first blade passage. In general, this is where the particle void disappeared and the vortex center became more difficult to identify with complete objectivity. Increased scatter beyond first blade passage is attributed to a reduced confidence in the measurement, but could also be due to an increased variability in the trajectory. The path of this vortex is considerably lower than that observed for Cases A-C.

### Calculated Results

In CAMRAD II, the rotor was trimmed to the measured  $C_T$  and zero 1/rev flapping angle. The multiple-trailer wake model with consolidation was used. The consolidation model uses the compression form with a linear dependence of the rollup fraction on wake age (Ref. 5). The assumed vortex core radius has a constant value of 80% of the mean chord. Two rotor revolutions of wake were simulated in the analysis. The intersections of vortex filaments with a plane at the laser light sheet location were extracted from the calculations for comparison with the measurements. Figure 13 shows the calculated wake geometry for Case A. The spanwise circulation distribution defined the sign of each of the sixteen filaments released from the edges of the aerodynamic panels of the blade. For this test condition, the advancing blade tip was negatively loaded producing a CCW tip vortex. The inboard filaments eventually roll up into a positive (CW) vortex located at the centroid of the inboard filaments. The roll up was chosen to occur at approximately  $\Psi_b=120$  degrees, which resulted in good airloads correlation in Ref. 5. The roll up age was scaled with  $r_G^2/G$ , where G is the total trailed strength and  $r_G$  is the second moment of the vorticity (Ref. 5). The velocity field in the simulated plane of the light sheet was calculated over a grid of 4 ft x 6 ft in increments of 0.02 ft in both directions (60,501 grid points). Figure 14 shows the calculated in-plane velocity and vorticity fields for Case A at  $\Psi_b=120$  degrees. The inboard vortices have significantly higher vorticity magnitudes than the vortices near the tip.

The calculated wake trajectories for Cases A-D are plotted in Figs. 15-18 for 15 degree increments in blade position. The CCW tip vortex and the CW primary (inboard) vortex are seen for Cases A-C. Evidence of the root vortex is also shown. The near-wake is represented by individual filaments which

eventually roll up into the primary vortex (recall Fig. 13).

Comparing Cases A and C (Figs. 15 and 17), the reduction in advance ratio produces a steeper trajectory for both the tip and inboard vortices. This result is reasonable since at higher speeds the wake is forced closer to the rotor tip path plane. Comparing Figs. 15 and 16, increasing thrust at advance ratio of 0.15 reduces the blade azimuth range of negative loading. The CCW vortex trajectory merges with the CW trajectory close to mid-span and from that point, only the CW trajectory exists. At an advance ratio of 0.10, increasing thrust essentially eliminates negative loading at the tip (compare Figs. 17 and 18) as shown by the lack of CCW vortices near the origin in Fig. 18. Decreasing advance ratio at  $C_T = 0.013$  also eliminates the negative loading (compare Figs. 16 and 18). Since Case D represents a conventional blade loading condition, the tip vortex roll-up model was also used as shown in Fig. 18. Using the tip vortex roll-up model forces a CW vortex to form at the blade tip.

### Correlation Results

Figures 19-22 overlay the measured and calculated wake trajectories for Cases A-D. Figure 19 shows that the calculated trajectory for the CCW vortex in Case A matches the measured trajectory in shape but is slightly lower in height. The CW vortex trajectory is not well matched. Note that the measured trajectory indicates roll up does not occur before  $\Psi_b < 120$  deg, confirming the adequacy of the assumption for the initiation of vortex roll up age used by the analysis. For Case B (Fig. 20), the calculations predict negative tip loading contrary to the measured initial positive tip loading. The calculated CW vortex trajectory passes through the cluster of points attributed to the vortex of unknown wake wage, but does not predict a second CW trajectory near the CCW trajectory as depicted in the data. The CCW vortex trajectory is captured in shape for Case C, but the calculated peak height above the blade is 30% too high compared with the measurements (Fig. 21). The calculated CW vortex trajectory is too low, but otherwise does a reasonable job of capturing the trajectory shape and the age at which roll up occurs. For Case D (Fig. 22), the roll-up model captures the initial trajectory of the tip vortex, but the peak height above the blade is 40% lower than measured and the calculated radial convection is much slower than the measured trajectory. For this case, the tip vortex roll-up model provides better correlation than the multiple trailer model, but neither is adequate for capturing the measured trajectory.

Both the calculated and measured wake trajectories exhibit similar trends when advance ratio is varied at fixed thrust or when thrust is varied at fixed advance ratio. The agreement is encouraging and warrants further study.

## Conclusions

The vortex wake trajectory from one rotor of a 0.25-scale V-22 tiltrotor was measured for four test conditions. Vortex wake images were acquired using laser light sheet flow visualization. Wake trajectories were constructed by extracting vortex positions from the video images. Wake trajectories were also calculated using CAMRAD II. Measured and calculated wake geometries were compared. Conclusions from this investigation are listed below.

1. For conventional (positive) tip loading or conditions where the blade tip loading is negative over the second quadrant of the disk, assigning a reference time to the vortices in the images is relatively straightforward.
2. Both the calculated and measured wake trajectories exhibit similar trends when advance ratio is varied at fixed thrust or when thrust is varied at fixed advance ratio.
3. The multiple-trailer model with consolidation provides good correlation with the measured wake trajectory of the tip vortex for  $C_T=0.087$ . The inboard vortex at this condition was not as well matched. At higher thrust, the agreement was poor.
4. Neither the tip vortex roll-up model nor the multiple-trailer model provided a good simulation of the wake trajectory of a tiltrotor blade with conventional (positive) tip loading.

## References

1. Young, L.A., Booth, E.R., Jr., Yamauchi, G.K., Botha, G., and Dawson, S., "Overview of the Testing of a Small-Scale Proprotor," American Helicopter Society 55th Annual Forum, Montreal, Canada, May 1999.
2. Yamauchi, G. K., Burley, C. L., Mercker, E., Pengel, K., and JanakiRam, R. D., "Flow Measurements of an Isolated Model Tilt Rotor," American Helicopter Society 55th Annual Forum, Montreal, Canada, May 1999.
3. Johnson, W., "Calculation of Tilt Rotor Aeroacoustic Model (TRAM DNW) Performance, Airloads, and Structural Loads," American Helicopter Society Aeromechanics Specialists' Meeting, Atlanta, Georgia, November 2000.
4. Johnson, W., "Calculation of the Aerodynamic Behavior of the Tilt Rotor Aeroacoustic Model (TRAM) in the DNW," American Helicopter Society 57th Annual Forum, Washington, D.C., May 2001.
5. Johnson, W., "Influence of Wake Models on Calculated Tiltrotor Aerodynamics," American Helicopter Society Aerodynamics, Acoustics, and Test and Evaluation Specialists Conference, San Francisco, California, January 2002.
6. Young, L.A., "Tilt Rotor Aeroacoustic Model (TRAM): A New Rotorcraft Research Facility," Heli Japan 98: American Helicopter Society Meeting on Advanced Rotorcraft Technology and Disaster Relief, Nagarafukumitsu, Gifu, Japan, April 1998.
7. Johnson, J.L. and Young, L.A., "Tilt Rotor Aeroacoustic Model Project," Confederation of European Aerospace Societies (CEAS), Forum on Aeroacoustics of Rotorcraft and Propellers, Rome, Italy, June 1999.
8. McCluer, M. S. and Johnson, J. L., "Full-Span Tiltrotor Aeroacoustic Model (FS TRAM): Overview and Initial Testing," American Helicopter Society Aerodynamics, Acoustics, and Test and Evaluation Specialists Conference, San Francisco, California, January 2002.
9. Johnson, W., "CAMRAD II, Comprehensive Analytical Model of Rotorcraft Aerodynamics and Dynamics," Johnson Aeronautics, Palo Alto, California, 1992-2002.
10. Johnson, W., "Technology Drivers in the Development of CAMRAD II," American Helicopter Society Aeromechanics Specialists Conference, San Francisco, California, January 1994.
11. Johnson, W., "Rotorcraft Aeromechanics Applications of a Comprehensive Analysis," Heli Japan 98: American Helicopter Society Meeting on Advanced Rotorcraft Technology and Disaster Relief, Gifu, Japan, April 1998.
12. Johnson, W., "A General Free Wake Geometry Calculation for Wings and Rotors," American Helicopter Society 51st Annual Forum, Fort Worth, Texas, May 1995.
13. Johnson, W., "Rotorcraft Aerodynamics Models for a Comprehensive Analysis," American Helicopter Society 54th Annual Forum, Washington, D.C., May 1998.



Figure 1. Full-span TRAM installed in NASA Ames 40- by 80-Foot Wind Tunnel. Acoustic traverse in foreground.

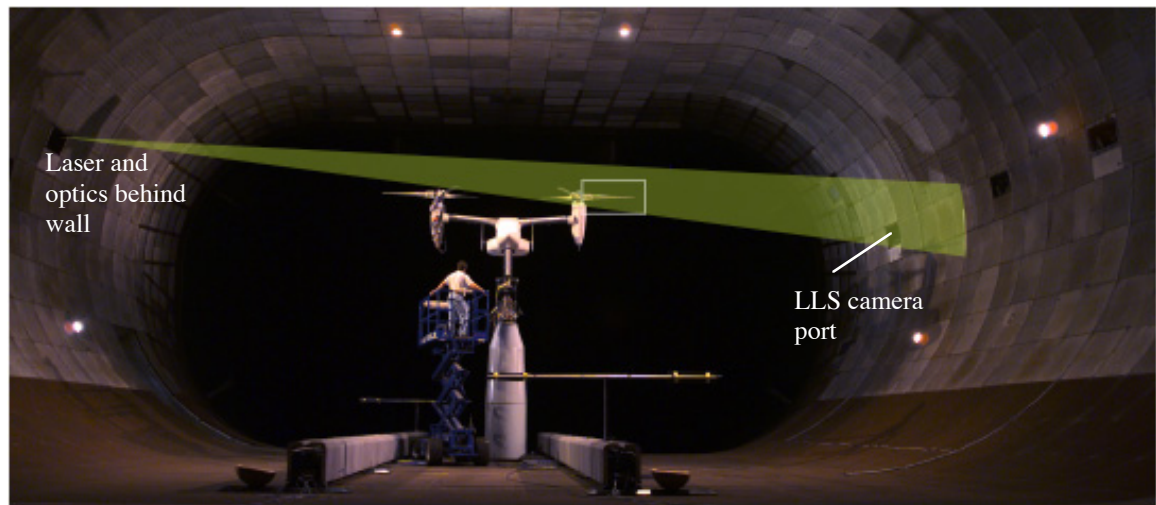


Figure 2. LLS projection across 40- by 80-Foot Wind Tunnel test section. White rectangle indicates camera field of view. View looking downstream.

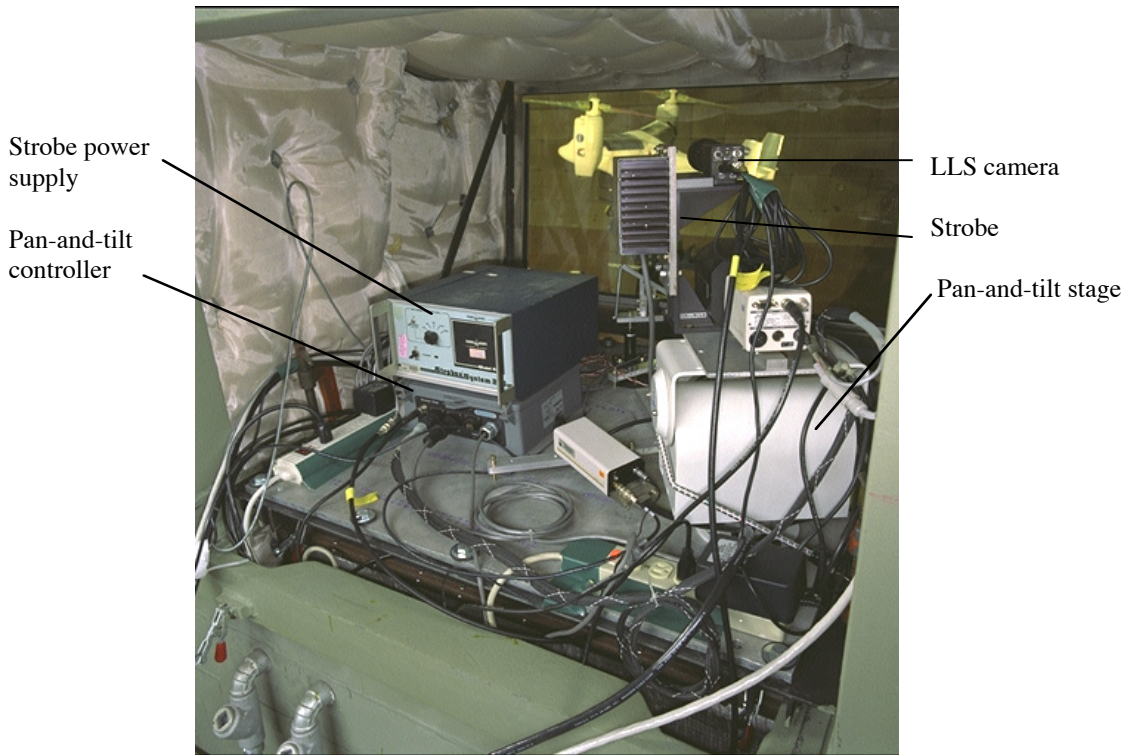


Figure 3. View of model from behind LLS camera.

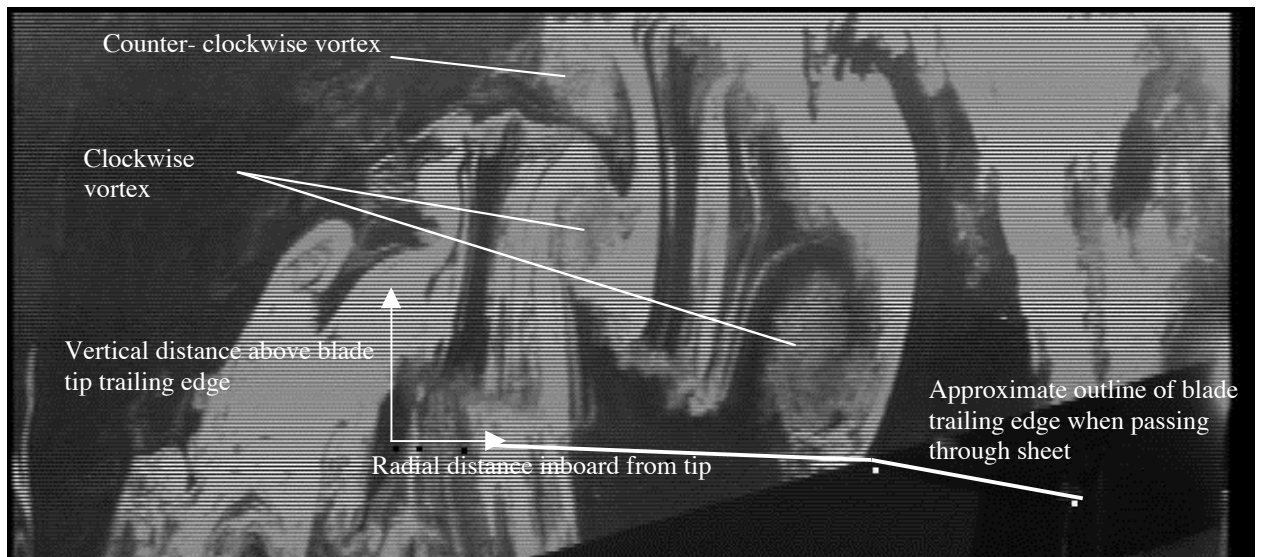


Figure 4. Sample LLS image. View from behind advancing side of left rotor. Coordinate system origin at blade tip trailing edge. Blade rotation is into paper.

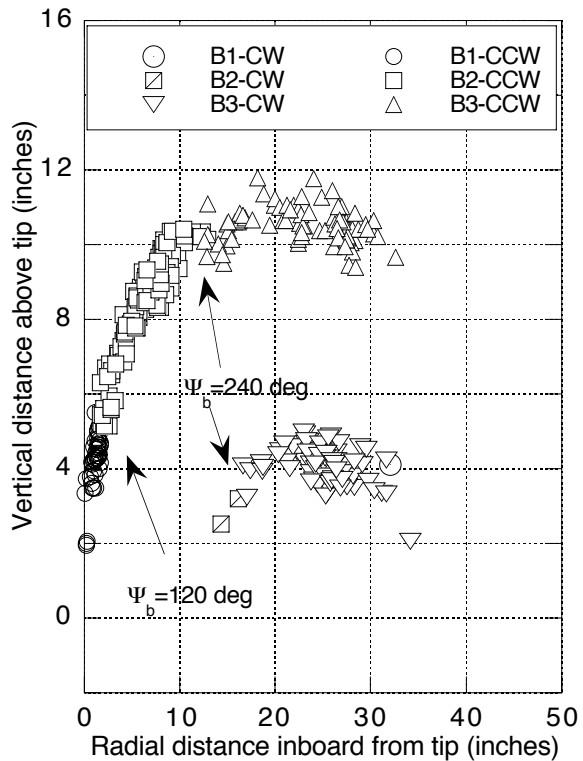


Figure 5. Case A.  $C_T = 0.0087$ ,  $\mu = 0.150$ .  
Measurements.

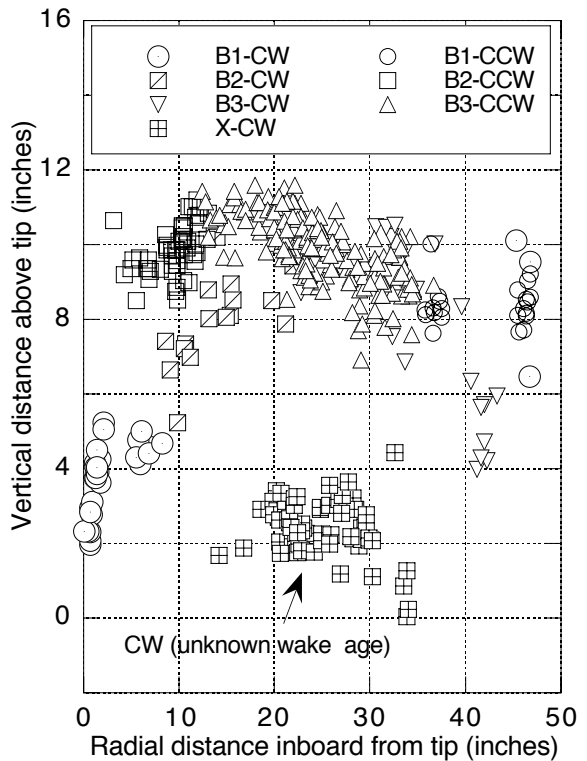


Figure 6. Case B.  $C_T = 0.0125$ ,  $\mu = 0.150$ .  
Measurements.

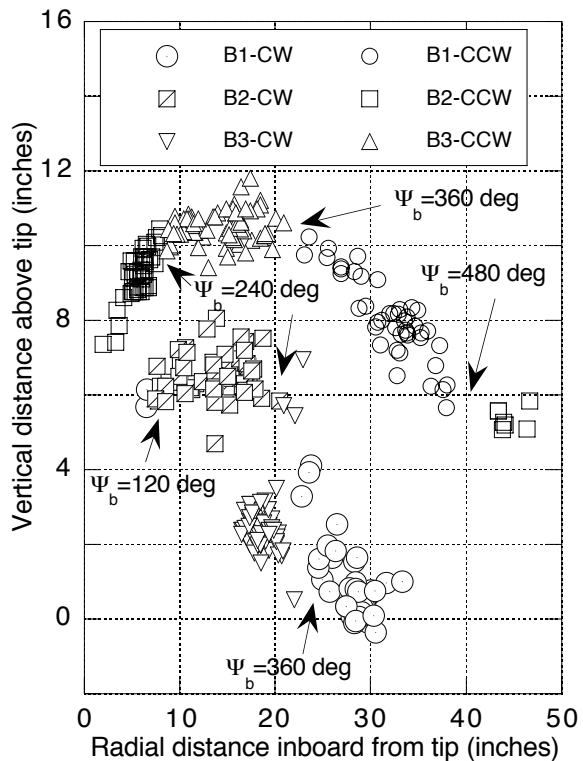


Figure 7. Case C.  $C_T = 0.0087$ ,  $\mu = 0.099$ .  
Measurements.

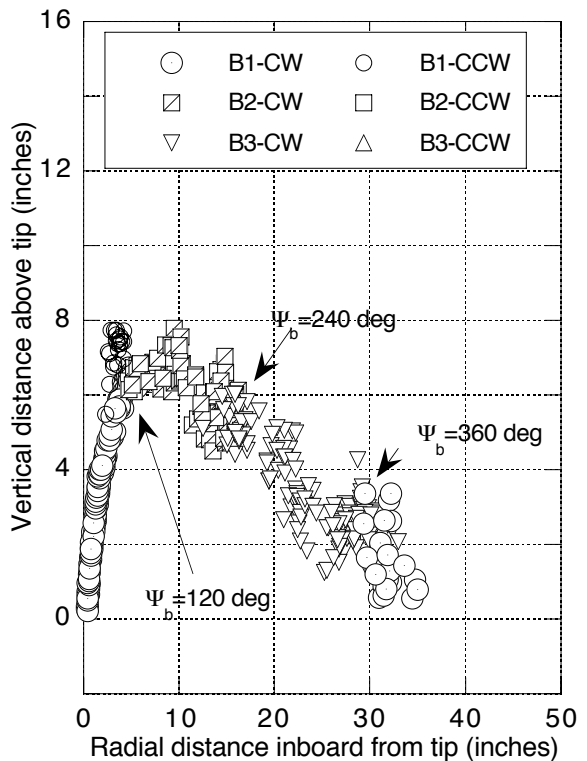


Figure 8. Case D.  $C_T = 0.0127$ ,  $\mu = 0.099$ .  
Measurements.

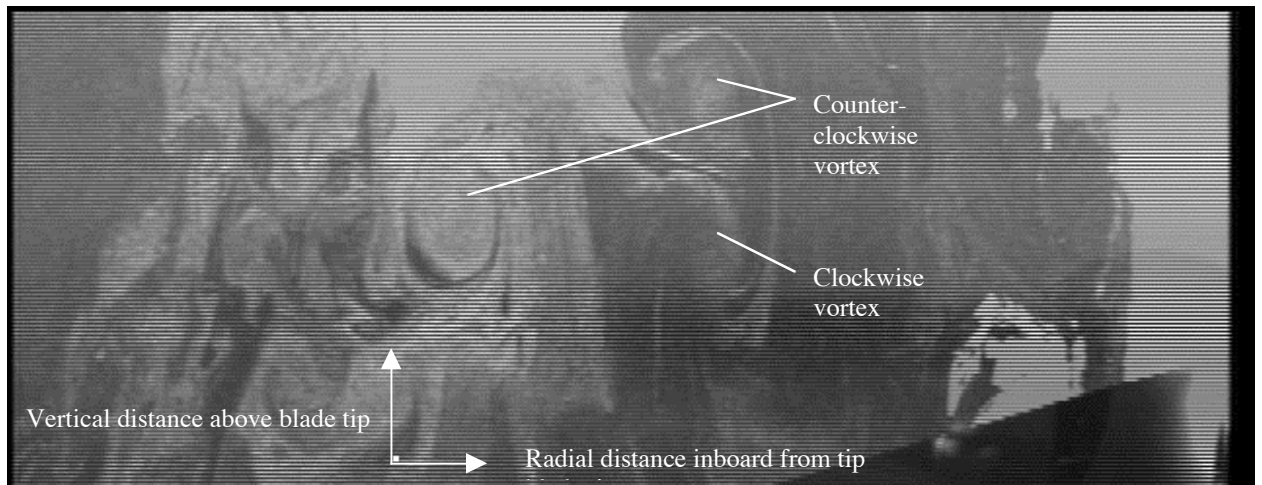


Figure 9. Case A.  $C_T = 0.0087$ ,  $\mu = 0.150$ . View from behind left-hand rotor on advancing side.

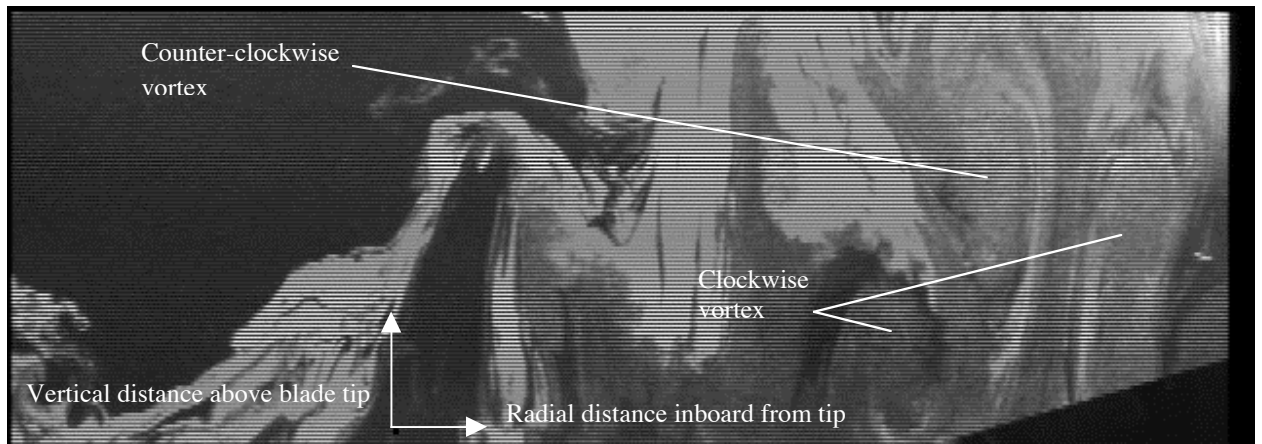


Figure 10. Case B.  $C_T = 0.0125$ ,  $\mu = 0.150$ . View from behind left-hand rotor on advancing side.

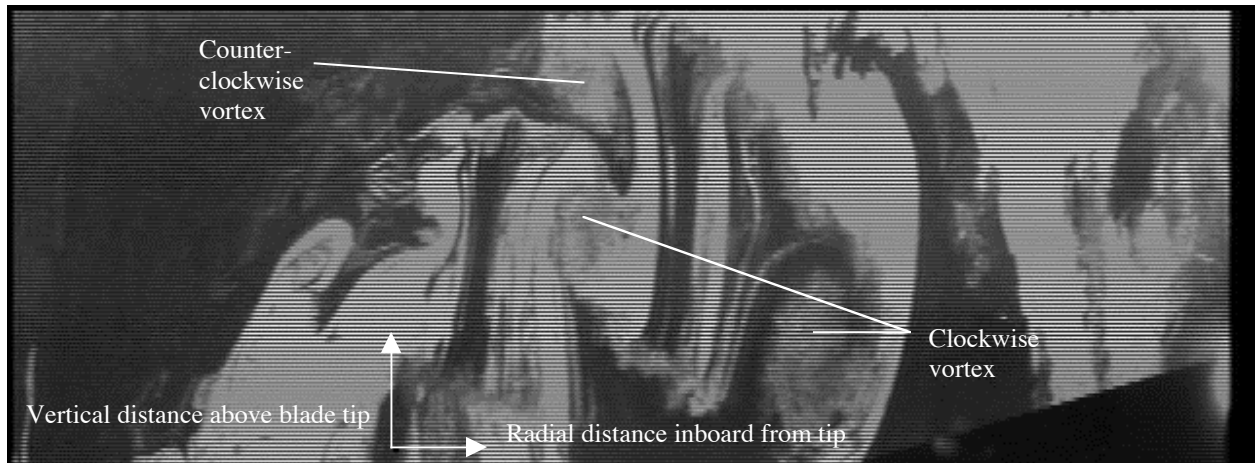


Figure 11. Case C.  $C_T = 0.0087$ ,  $\mu = 0.099$ . View from behind left-hand rotor on advancing side.

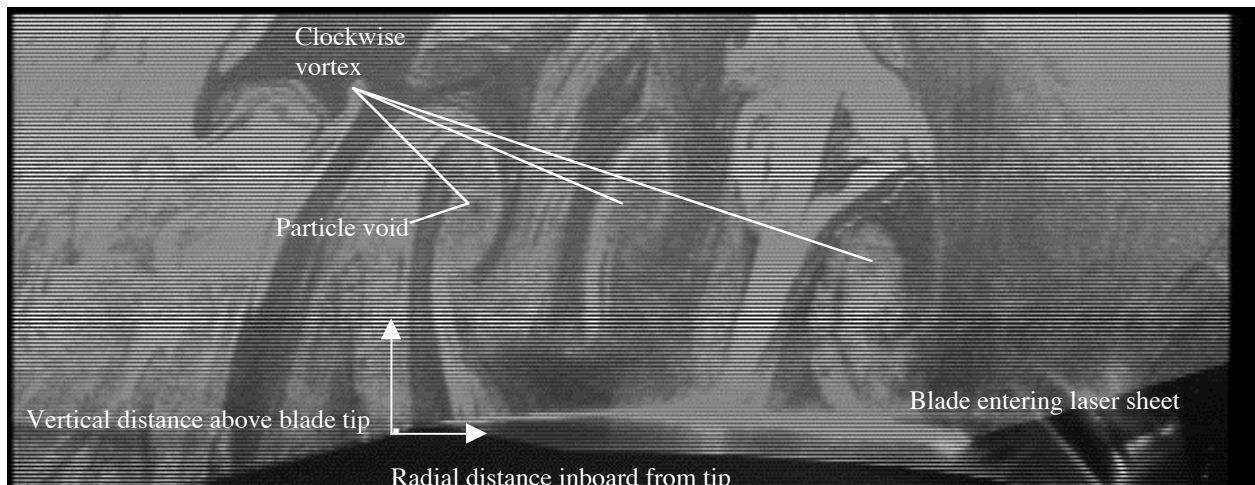


Figure 12. Case D.  $C_T = 0.0127$ ,  $\mu = 0.099$ . View from behind left-hand rotor on advancing side.

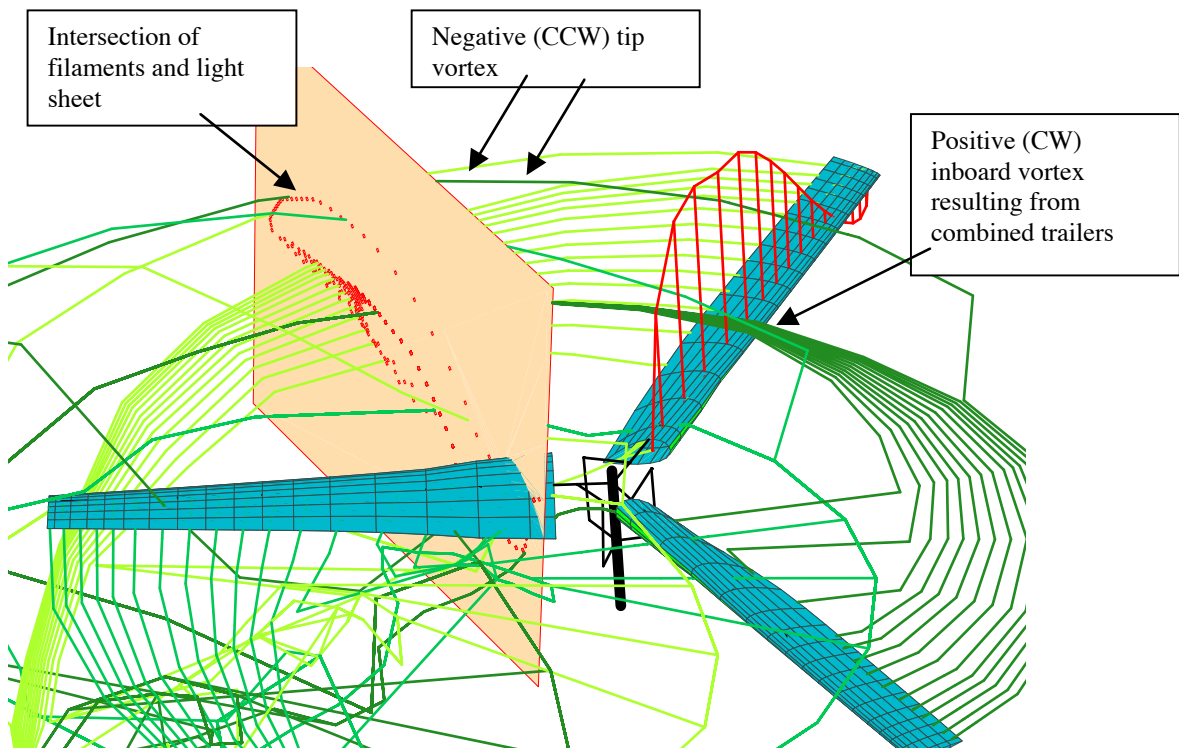


Figure 13. Case A.  $C_T = 0.0087$ ,  $\mu = 0.150$ . Calculated vortex filament intersections with plane of laser light sheet.

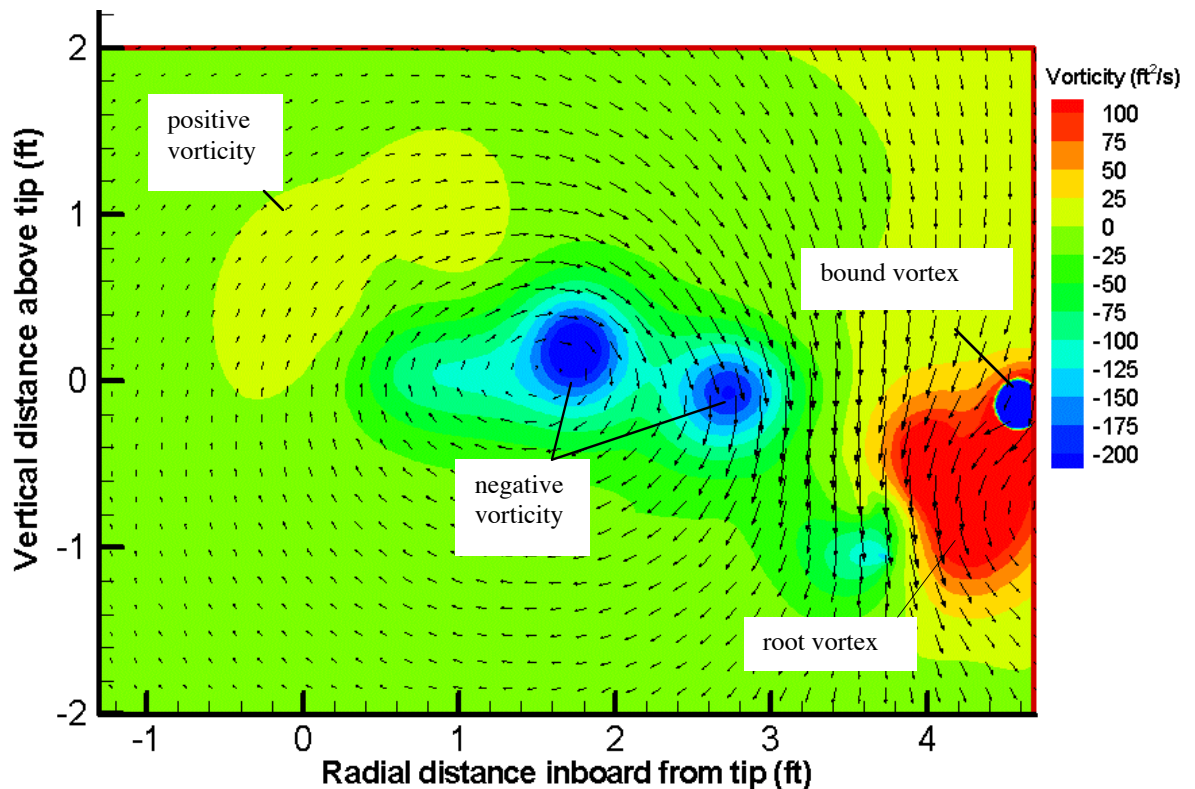


Figure 14. Case A.  $C_T = 0.0087$ ,  $\mu = 0.150$ . Blade position=120 degrees. Every 8<sup>th</sup> vector shown. Velocity and vorticity field in simulated laser light sheet plane.

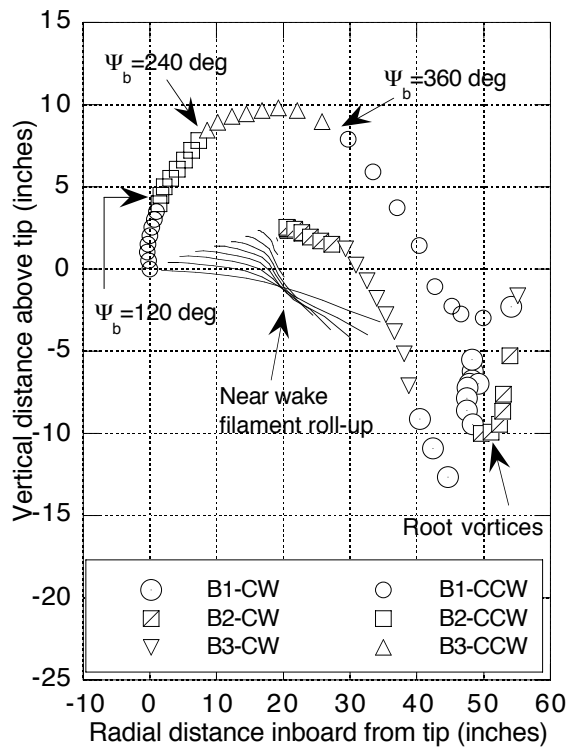


Figure 15. Case A.  $C_T=0.0087$ ,  $\mu=0.150$ . Calculations.

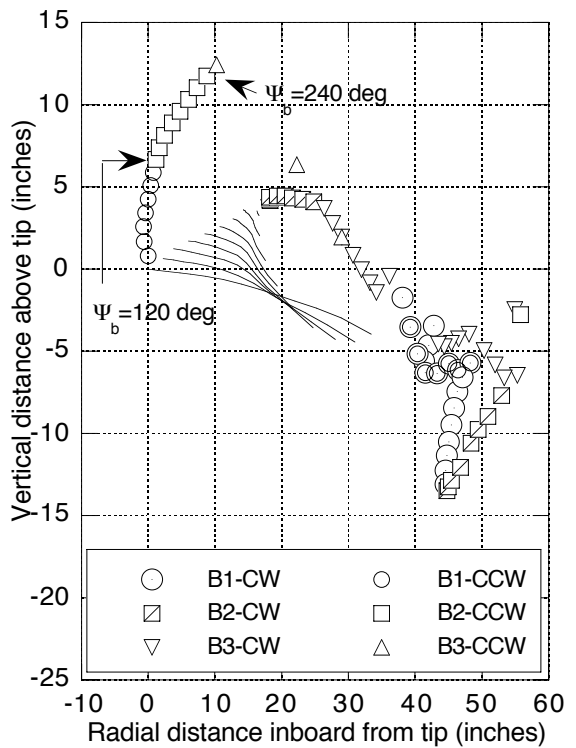


Figure 16. Case B.  $C_T=0.0125$ ,  $\mu=0.150$ . Calculations.

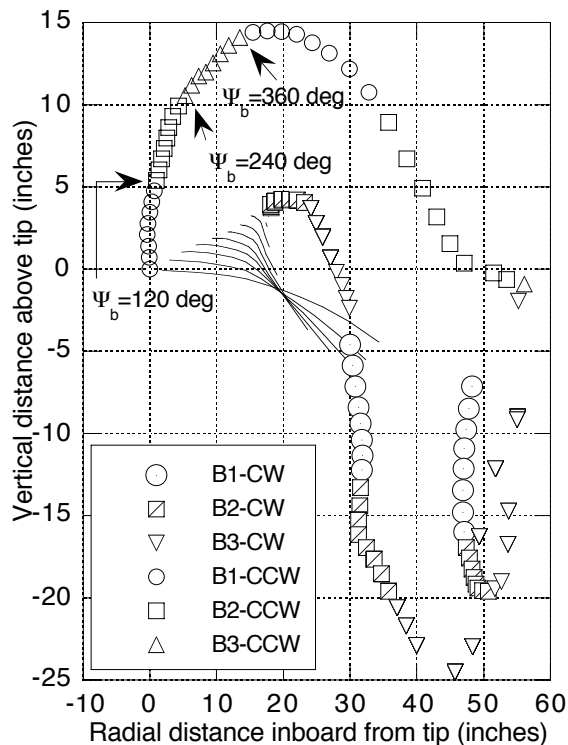


Figure 17. Case C.  $C_T=0.0087$ ,  $\mu=0.099$ . Calculations.

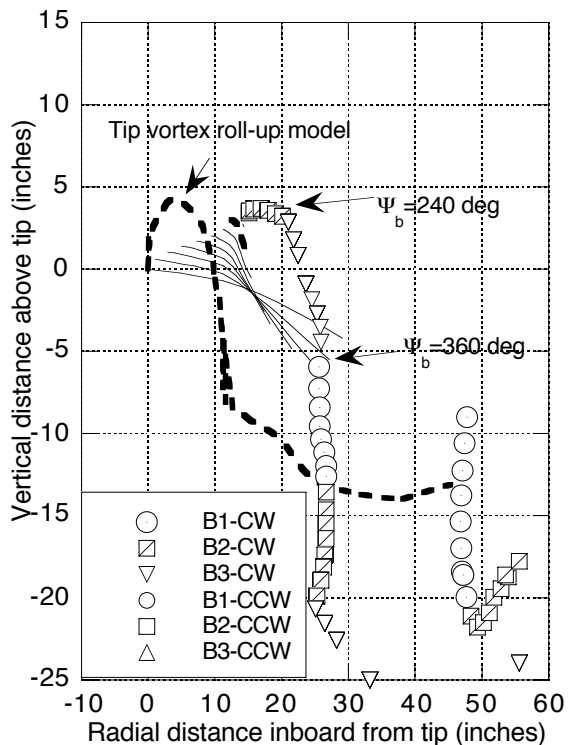


Figure 18. Case D.  $C_T=0.0127$ ,  $\mu=0.099$ . Calculations.

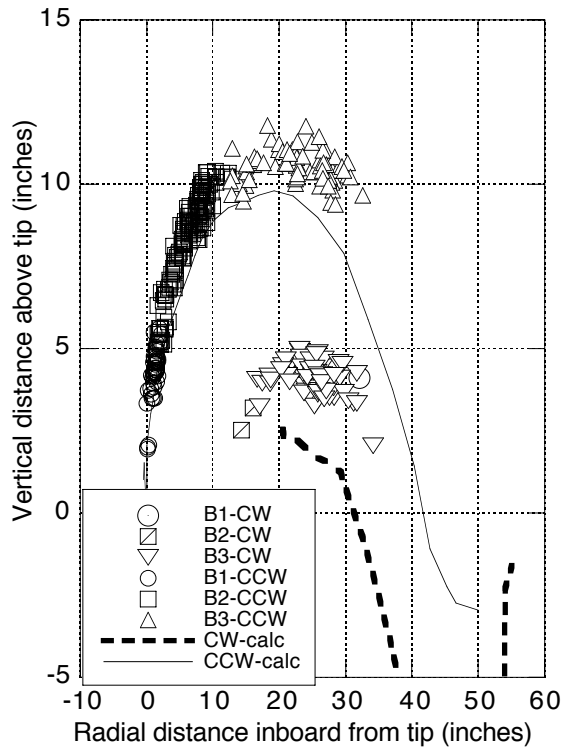


Figure 19. Case A.  $C_T = 0.0087$ ,  $\mu = 0.150$ . Correlation.

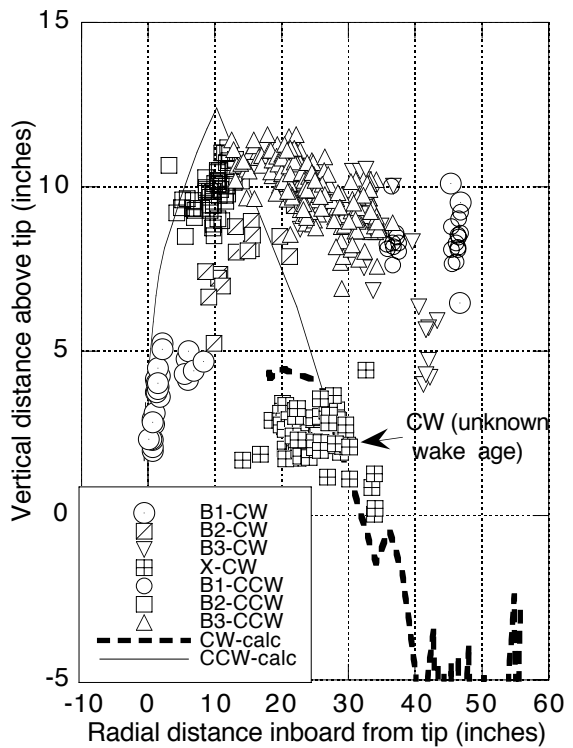


Figure 20. Case B.  $C_T = 0.0125$ ,  $\mu = 0.150$ . Correlation.

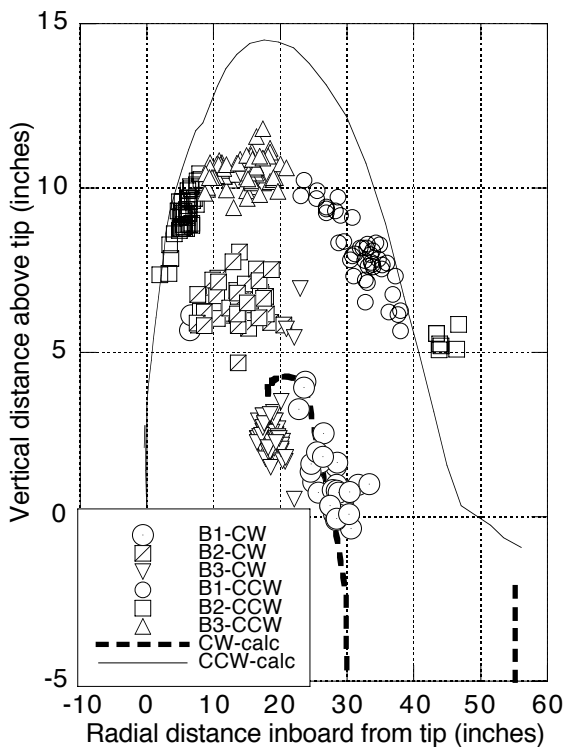


Figure 21. Case C.  $C_T = 0.0087$ ,  $\mu = 0.099$ . Correlation.

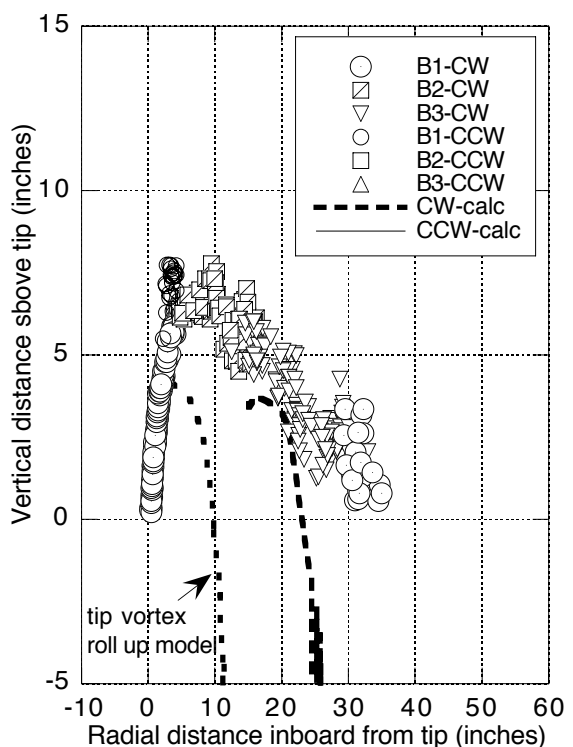


Figure 22. Case D.  $C_T = 0.0127$ ,  $\mu = 0.099$ . Correlation.